REVIEWS

Review of phonons in moiré superlattices

Zhenyao Li[1, 2], Jia-Min Lai[1, 2, †], and Jun Zhang[1, 2, 3, †]

[1]State Key Laboratory of Superlattices and Microstructures, Institute of Semiconductors, Chinese Academy of Sciences, Beijing 100083, China

[2]Center of Materials Science and Optoelectronics Engineering, University of Chinese Academy of Sciences, Beijing 100049, China

[3]CAS Center of Excellence in Topological Quantum Computation, University of Chinese Academy of Sciences, Beijing 100049, China

Abstract: Moiré patterns in physics are interference fringes produced when a periodic template is stacked on another similar one with different displacement and twist angles. The phonon in two-dimensional (2D) material affected by moiré patterns in the lattice shows various novel physical phenomena, such as frequency shift, different linewidth, and mediation to the superconductivity. This review gives a brief overview of phonons in 2D moiré superlattice. First, we introduce the theory of the moiré phonon modes based on a continuum approach using the elastic theory and discuss the effect of the moiré pattern on phonons in 2D materials such as graphene and MoS_2. Then, we discuss the electron–phonon coupling (EPC) modulated by moiré patterns, which can be detected by the spectroscopy methods. Furthermore, the phonon-mediated unconventional superconductivity in 2D moiré superlattice is introduced. The theory of phonon-mediated superconductivity in moiré superlattice sets up a general framework, which promises to predict the response of superconductivity to various perturbations, such as disorder, magnetic field, and electric displacement field.

Key words: moiré pattern; moiré phonon; electron–phonon coupling; superconductivity

1. Introduction

Moiré pattern refers to a geometrical design produced when a set of curved or straight lines is superposed onto another set, resembling water with ripples, which is the French meaning for "moiré", as shown in Fig. 1(a)[1]. In physics, the moiré pattern is a kind of novel phenomenon for various materials especially for two-dimensional (2D) materials, which occurs when the angle or lattice parameter of the 2D materials mismatch that of another layer[2, 3]. The moiré pattern forms a larger periodic unit than the original one, called moiré superlattice, which has been used to engineer the optical properties or electronic structure of 2D materials[4] and generate a series of novel phenomena. For example, replica Dirac cones and Van Hove singularities appear in twisted bilayer graphene (tBLG)[5, 6] and superconductivity and Mott insulators can be observed[7]. Interlayer excitons are formed in moiré superlattices generating new optical selection rules, resonant energy, dynamics, and diffusion properties which can be controlled via the twist angle[8–11]. Intriguingly, the moiré pattern introduces periodic potential which affects not only the electronic structure but also the properties of phonons. In 2008, Yan *et al.* used density-functional perturbation theory to calculate phonon dispersions in tBLG, twisted monolayer, and trilayer graphene (tMLG and tTLG)[12]. The phonon modes of the bottom layer and the top layer are coupled to form layer-asymmetric and -symmetric modes with the bilayer graphite's AB stacking (Bernal stacking). The optical phonon E_{2g} mode at Γ was found to split in twist graphene[12, 13]. The relation between phonon modes and twist angles was also observed in graphene-hexagonal boron nitride (hBN) heterojunction by Raman spectroscopy to characterize the rotational order of the van der Waals heterostructures[14].

It was reported that the moiré interlayer potential can fold the superlattice zone and cause miniband generation in the spectrum of phonons in twist 2D materials[15–18]. The concept of moiré phonons was introduced in twisted bilayer MoS_2 (tBLM)[19] in 2018, where the lattice structures of crystallographic superlattices and moiré superlattices were defined to analyze the phonon folding effect in twist bilayer 2D materials. The vectors in the upper and lower monolayers are defined as $m\boldsymbol{a}_1 + n\boldsymbol{a}'_1$ and $m\boldsymbol{a}_2 + n\boldsymbol{a}'_2$, where $\boldsymbol{a}_1$, $\boldsymbol{a}'_1$ and $\boldsymbol{a}_2$, $\boldsymbol{a}'_2$ are the lattice basis of the top layer and the bottom layer, respectively, and (m,n) is a pair of coprime numbers. When the twist angle θ makes the period of the upper monolayer and that of the lower monolayer just match, the crystallographic superlattice can be defined with the fundamental vectors: $L_1 = m\boldsymbol{a}_1 + n\boldsymbol{a}'_1$ and $L_2 = (m + n)\boldsymbol{a}_2 + m\boldsymbol{a}'_2$ shown in Fig. 1(b) as a green parallelogram, where $(m,n) = (5,7)$. In addition, there is a moiré period potential in twist bilayer 2D materials and fundamental vectors of moiré superlattice can be defined by lattice vectors $\boldsymbol{L}_1^M$ and $\boldsymbol{L}_2^M$, and the lattice constant is $|\boldsymbol{L}_1^M| = |\boldsymbol{L}_2^M| = \frac{a}{2\sin(\theta/2)}$ shown in Fig. 1(b) as a red parallelogram. The moiré superlattice is only relevant for twist angle θ. The reciprocal lattice is defined according to the crystallographic superlattice and moiré superlattice basis vectors as shown in Fig. 1(c), where we can obtain the Brillouin zone. There is a folding effect of the Brillouin zone in the superlattice, and phonons are modulated. The moiré phonons are additional phonons modulated by moiré superlattices, rather than phonons associated with crystallographic superlattices. Moiré phonons have various unique properties. The moiré phonons in tBLM observed by Raman spectra show some characteristics
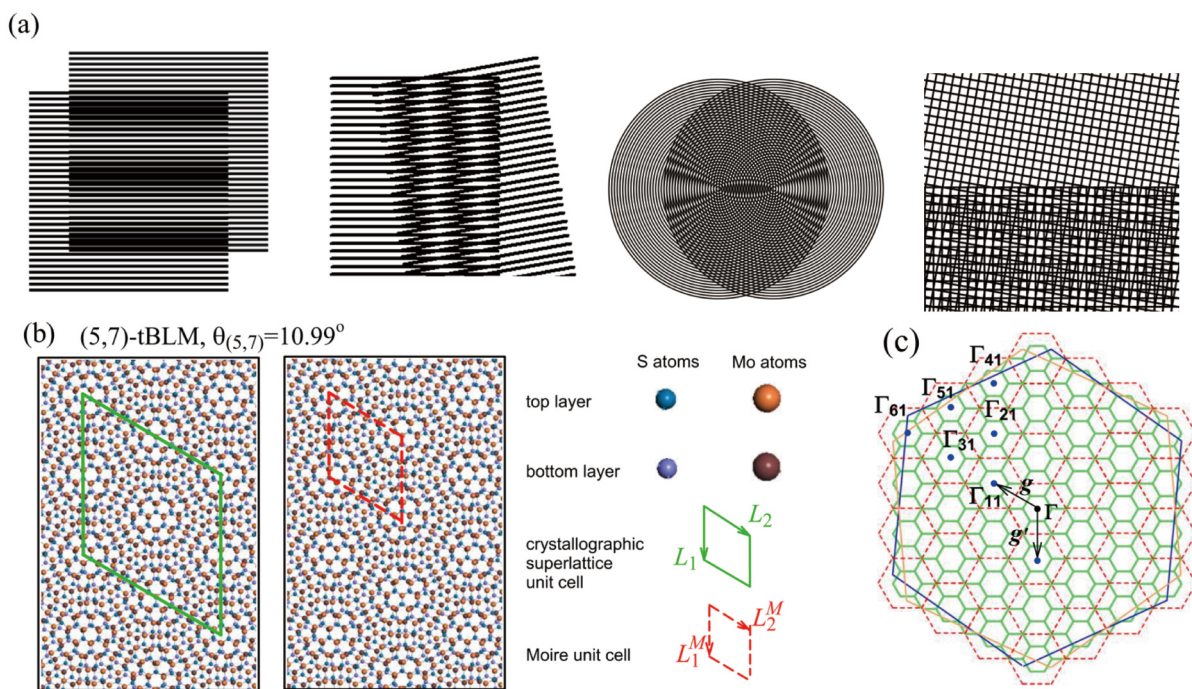
Fig. 1. (Color online) (a) Moiré pattern obtained by the overlapping of two similar fringes with different displacement and twist angles[27]. (b) Crystallographic superlattice and moiré superlattice in (5,7)-tBLM with $\theta = 10.99°$. The green solid parallelogram represents the crystallographic superlattice unit cell and the red dashed parallelogram represents the moiré superlattice unit cell. (c) The reciprocal lattice of (5,7)-tBLM. The green and red regular hexagons correspond to the Wigner-Seitz primitive cells of the crystallographic superlattice and moiré superlattice, and the orange and blue hexagons represent the first Brillouin zone of the bottom and top MoS_2, respectively. Reproduced with permission from Ref. [19]. Copyright 2018, ACS Publications.

such as θ-dependent frequency, narrow linewidth, and weak intensity[19]. The effects of the moiré superlattice structure on the in-plane acoustic moiré phonon spectrum in tBLG were investigated and it was found that only in-plane asymmetric modes are influenced by moiré interlayer potential[20]. Besides, a low-energy continuum mode for moiré phonons was promoted, which describes phonon renormalization in moiré superlattice well and is agree with the experimental results[21].

Specifically, optical phonon moiré modes were shown fairly coupled to the flat bands strongly, which makes an important impact on the physics of 2D materials. For example, in 2018, phonon-mediated superconductivity based on electron–phonon coupling (EPC) was analyzed theoretically and it is found that phonons give rise to electron–electron attractive interactions in superconducting pairing[22]. This phonon-mediated electron–electron attraction can theoretically lead to the superconducting enhancement in the moiré superlattice[23] and the correlation between experimentally observed robust superconductivity and EPC has been theoretically analyzed[24]. For the research on the thermoelectricity of tBLGs, Raman spectra were used to reflect various twisted angles and the Seebeck coefficient exhibits twist angle dependence due to the hybridization of electronic and phononic bands of two graphene layers[25, 26]. These studies provide references for the design of rotation-tunable electronic devices.

In this review, the effective continuum theory is introduced to calculate relaxed lattice structure and moiré phonon dispersion can be obtained. Furthermore, in 2D materials, we take tBLGs and tBLMs as examples to discuss the moiré phonon reflected by Raman spectra, and next, the renormalization of moiré phonons depending on the change in moiré pattern is shown. Then, electron–phonon and exciton–phonon coupling and the related thermoelectricity in the moiré superlattice are shown. In addition, electron–phonon interaction depending on vibrational and electronic structures in the lattice can be modulated by moiré patterns leading to superconductivity. The comprehension of moiré phonons is deep and this is expected to carve out a new path to the quantum devices of 2D materials.

2. Moiré phonons in 2D materials

Twisted multilayer superlattices can produce moiré patterns and create moiré phonons by periodic interlayer interaction potentials. The lattice symmetry in moiré patterns is modified by different interlayer vibration modes. Moiré interlayer potential only influences the in-plane asymmetric modes in AB-stacked tBLG, where the original linear phonon dispersion is broken down into minibands separated by gaps while the in-plane symmetric modes with their linear dispersion are almost not influenced. In tBLMs, the angle-dependent frequency of moiré phonons can probe the phonon dispersions in monolayer constituents due to the weak interlayer coupling. Besides, phonon spectra renormalized are also found in reconstructed MoS_2 moiré superlattices. In this section, we will introduce the theoretical model of moiré lattice in twisted bilayer lattices, moiré phonon spectrum in tBLGs or tBLMs, and phonon renormalization.

2.1. Moiré phonons in tBLMs

The first experimental observation of moiré phonons was in tBLMs[19]. Under the effect of the periodic potential in moiré superlattice, the moiré phonons of the MoS_2 composition show unique properties, which can be detected by Ra-
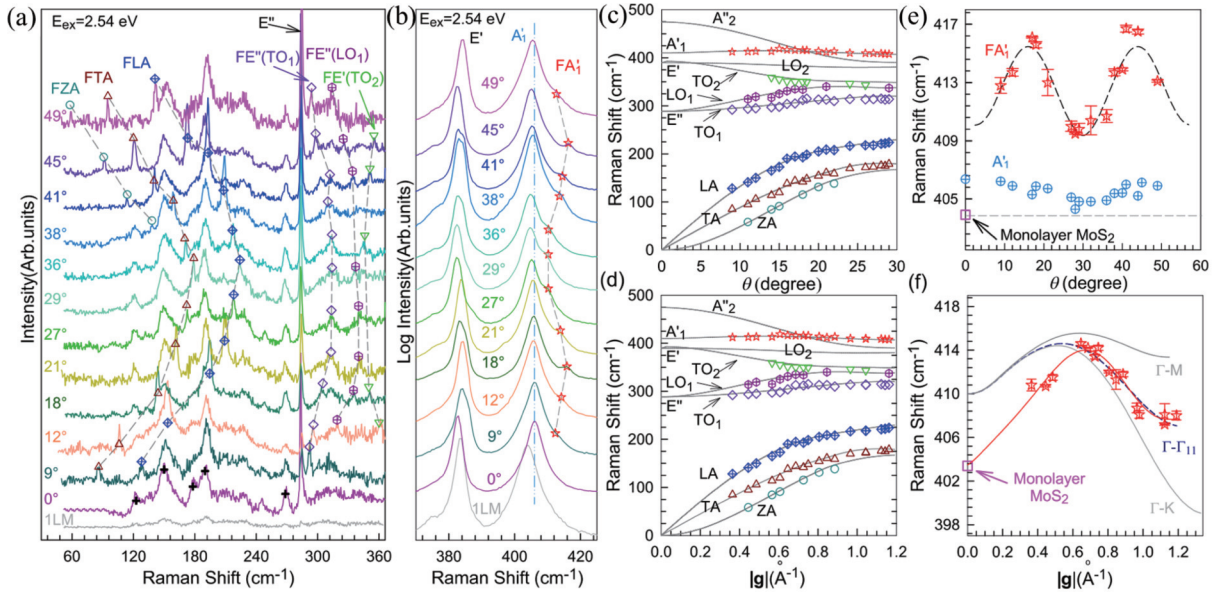
Fig. 2. (Color online) Raman spectra of tBLMs and monolayer MoS$_2$. The region of (a) is 50–365 cm^{-1} and (b) is 370–425 cm^{-1}. Raman modes in various phonon branches are labeled by different colors and symbols. (c, d) The experimental and calculated frequencies of moiré phonons vary with |g| and θ. The solid lines and the scatter symbols are theoretical and experimental results, respectively. (e, f) The peak position of FA_1' mode vary with |**g**| and θ. The peak position of A_1'-related branch of the monolayer MoS$_2$ (pink square) and various stacked BLMs (crossed circles) are also shown in (e). In (f), the theoretical phonon dispersion of A_1'- related branch along the Γ−M and Γ−K directions in the monolayer MoS$_2$ are shown as gray lines and the phonon dispersion of A_1'- related branch of the monolayer MoS$_2$ along **g** is shown as a dashed line. The stars are the experimental peak position of FA_1' in tBLMs. Reproduced with permission from Ref. [19]. Copyright 2018, ACS Publications.

man spectroscopy. These Raman modes related to moiré phonons correspond to zone-center phonons in tBLMs, which are folded from the off-center phonons in monolayer MoS$_2$. Figs. 2(a) and 2(b) show the Raman spectra of tBLMs. Compared to monolayer MoS$_2$, in the Raman spectra of 3R-stacked BLM (twist angle $\theta = 0°$), the Raman modes associated with the second-order Raman scattering of the longitudinal acoustic (LA), longitudinal optical (LO), transverse acoustic (TA), transverse optical (TO), and out-of-plane acoustic (ZA) phonons at K and M points of Brillouin zones were observed. These modes have been observed in other tBLMs, independent of θ, as shown by the crosses. There are six θ-dependent Raman modes in the range of 50–365 cm^{-1}, which are assigned to the moiré phonon mode associated with the FE''(TO$_2$), FE''(LO$_1$), FE''(TO$_1$), FLA, FZA, and FTA branches formed by the folding of phonons related to E''(TO$_2$), E''(LO$_1$), E''(TO$_1$), LA, ZA, and TA in monolayer MoS$_2$. In addition, a weak θ-dependent moiré phonon mode (FA_1') can be observed on the high-wavenumber side of each A_1' peak (~410 cm^{-1}). The Raman shift of the moiré phonons depending on twist angle θ and the size of moiré reciprocal lattice vector |g| are extracted in Figs. 2(c) and 2(d), respectively. The Raman scattering peaks corresponding to these moiré phonons share several common features, such as θ-dependent frequency, narrow linewidth, and weak intensity, so it is easy to distinguish the moiré phonons from other phonon modes.

The peak position of A_1' mode is sensitive to the θ and the function of the peak position of FA_1' mode versus θ is V-shaped. While the peak position of A_1' mode in tBLMs does not show that trend (Fig. 2(e)). It is because there is a perturbation in the interlayer coupling introduced by the periodic moiré potential in tBLMs. According to the relation between θ and dependent basic vectors of moiré reciprocal lattices |g| = 2$b$sin(θ/2), the A_1' dispersions along Γ−M and Γ−K directions can be transformed to A_1' phonon frequencies varying with |g| shown in Fig. 2(f). It is found that when |g| is over ~0.6 Å^{-1}, the changing trend of the Raman shift of FA_1' mode obtained experimentally resembles that of A_1' mode obtained theoretically, while when |g| is below ~0.6 Å^{-1} the trends do not match. Considering the peak position of A_1' mode in the monolayer is lower than the calculated result at Γ, the actual phonon dispersion is supposed to decrease toward Γ more sharply than the interpolated phonon dispersion. The phonon dispersions of the A_1'-related branch in the monolayer MoS$_2$ can be mapped from the θ-dependent peak position of FA_1' in tBLMs by changing the twist angle.

Reconstructed moiré superlattices affect the renormalization of moiré phonons under small angle changes. The phonon spectra evolve rapidly owing to the ultra-strong coupling between different phonon modes and atomic reconstructions of the moiré pattern in a range of small twist angles θ. Quan et al. calculated the evolution of moiré phonon modes by a low-energy continuum model, which agrees well with the experimentally observed lattice reconstruction[21]. The low energy continuum model method proposed by MacDonald and Bistritzer[6, 28] is employed to calculate the electron and phononic systems of the moiré superlattice. The model results in a total of 126 modes, and 18 moiré reciprocal lattice modes are folded and vary with θ. The frequencies of the calculated mode are shown in Figs. 3(a) and 3(b). In both rigid and relaxed systems, the layer breathing (LB) mode has only a weak twist angle dependence (Fig. 3(b)). It can be recognized that the LB modes in both cases are similar by comparing the calculated results without (Fig. 3(a)) and with (Fig. 3(b)) lattice relaxation. The calculation and measurement of the LB patterns are perfectly matched at all θ. Furthermore, at small twist angles, the lattice reconstruction results in a degenerate S-mode frequency shift and matches the meas-
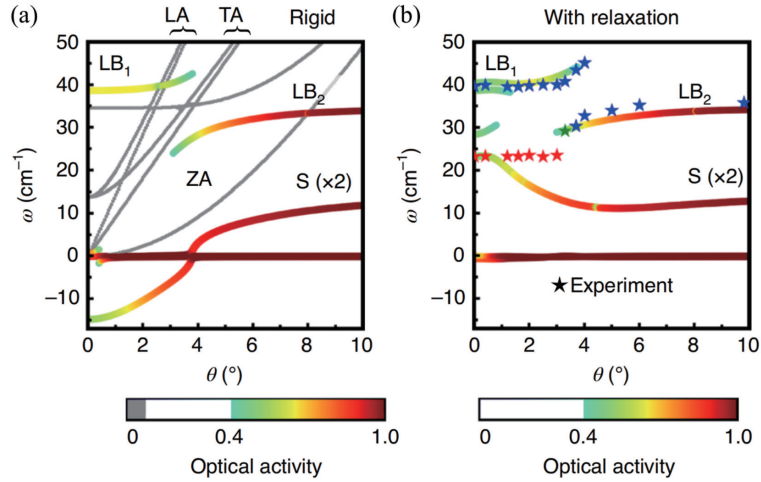
Fig. 3. (Color online) (a, b) Calculated the low-energy evolution of phonon modes developed twist angle θ at Γ. Color bars based on optical activity project the phonon eigenmodes onto the central Γ point. Optically inactive modes are shown by grey lines in (a) entirely originating at neighboring Γ points. Reproduced with permission from Ref. [21]. Copyright 2021, Springer Nature.
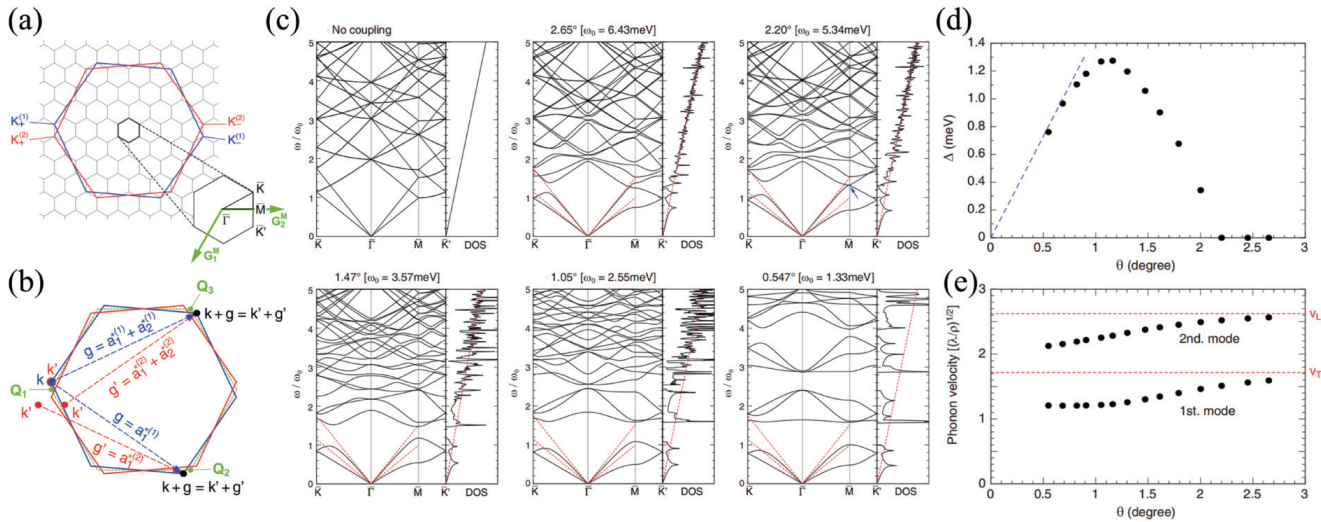

Fig. 4. (Color online) (a) The moiré pattern as seen in the tBLG. The first Brillouin zones of layers 1 and 2 are shown as two large hexagons, and small hexagons are moiré Brillouin zones of the tBLG. (b) Schematic illustrating the coupling of interlayer from the initial $\boldsymbol{k}$ in layer 1 (given by as $K_+^{(1)}$) to the three $\boldsymbol{k}'$ points in layer 2 in an undistorted tBLG, where $\boldsymbol{k}$ is a two-dimensional Bloch wave vector. Reproduced with permission from Ref. [30]. Copyright 2020, American Physical Society. (c) Phonon dispersion in the inner asymmetric mode ($\boldsymbol{u}^-$) under different twist angles θ. (d) The gap width between the third and second branches of the phonon of $\boldsymbol{u}^-$ mode as a function of θ. The blue dashed line indicates the linear dependence on θ. (e) Group velocities of the second and first $\boldsymbol{u}^-$ phonon modes dependent on θ. The velocities of transverse (v_t) and longitudinal (v_l) phonons in monolayer graphene are represented by horizontal dashed lines. Reproduced with permission from Ref. [20]. Copyright 2018, American Physical Society.

urements. This model theoretically links the reconstructed moiré superlattices to phonon renormalization and promotes a unified and comprehensive unified understanding of the electrical and optical properties and structure of moiré superlattices.

2.2. Moiré phonons in tBLGs

A generally effective continuum theory has been proposed to describe moiré phonons in tBLGs[20]. Firstly, the lattice geometry is introduced to describe the change rule of the displacement vector of the lattice. Based on AB stacked bilayer graphene, the stacking geometry is specified by the rotation angle of layer 2 relative to layer 1 as shown in Figs. 4(a) and 4(b), where the first Brillouin zone defined by $\boldsymbol{G}_i^M$, i.e. the moiré reciprocal lattice vectors. Under small-angle rotations, long-period moiré beating modes are generated

due to the mismatch of the lattice periods, where the spatial period can be estimated.

Our goal is to get phonon modes and phonon frequency ω. $\boldsymbol{u}^{(l)}(\boldsymbol{r})$ is defined as a displacement vector of the lattice with position $\boldsymbol{r}$ and layer number l, and perturbational excitation $\delta\boldsymbol{u}^-$ is introduced to describe phonon modes. The Euler-Lagrange equation is given to obtain the optimized relaxed state solution minimizing the sum of the interlayer binding energy and the elastic energy of tBLG[20]

$$\frac{1}{2}(\lambda + \mu)\left(\frac{\partial^2 u_x^-}{\partial x^2} + \frac{\partial^2 u_y^-}{\partial x \partial y}\right) + \frac{\mu}{2}\left(\frac{\partial^2 u_x^-}{\partial x^2} + \frac{\partial^2 u_x^-}{\partial y^2}\right) +$$
$$\sum_{j=1}^{3} 2V_0 \sin\left[\boldsymbol{a}_j^* \cdot \boldsymbol{u}^- + \boldsymbol{G}_j^M \cdot \boldsymbol{r}\right] a_{jx}^* = \frac{1}{2}\rho \frac{\mathrm{d}^2 u_x^-}{\mathrm{d}t^2}, \quad (1)$$

$$\frac{1}{2}(\lambda + \mu)\left(\frac{\partial^2 u_y^-}{\partial y^2} + \frac{\partial^2 u_x^-}{\partial x \partial y}\right) + \frac{\mu}{2}\left(\frac{\partial^2 u_y^-}{\partial x^2} + \frac{\partial^2 u_y^-}{\partial y^2}\right) +$$

$$\sum_{j=1}^{3} 2V_0 \sin\left[\boldsymbol{a}_j^* \cdot \boldsymbol{u}^- + \boldsymbol{G}_j^M \cdot \boldsymbol{r}\right] a_{jy}^* = \frac{1}{2}\rho\frac{\mathrm{d}^2 u_y^-}{\mathrm{d}t^2}, \quad (2)$$

where $\boldsymbol{u}^\pm = \boldsymbol{u}^{(1)} + \boldsymbol{u}^{(2)}$, $u_{ij}^{(l)}$ is the strain tensor, λ and μ are typical values of Lamé factor of graphene[29], V_0 is the interlayer interacting potential, $\boldsymbol{a}_i$ and $\boldsymbol{a}_i^*$ are respectively primitive and reciprocal lattice vectors of layer i, a is lattice constant, a_{jx}^* is the l component of $\boldsymbol{a}_j$, and ρ is the density of materials. The phonon dispersion with twist angles θ calculated by the Euler-Lagrange equation is shown in Fig. 4(c), in which the in-plane acoustic phonon modes of graphene are renormalized and dispersions show superlattice minibands. There is a gap between the lowest two bands and the rest of the spectra in the lower twist angles as shown in Fig. 4(c)[20]. The full gap opens when the twist angle $\theta < \theta_c$, where the critical angle $\theta_c \approx 2.20°$. The spectral gaps are also found between the ninth, eighth, sixth, and fifth modes when θ takes the minimum value. In Fig. 4(d), the gap width between the third and the second branches is plotted as a function of θ. As the θ increases, the gap size is converged and approaches a constant value. The phonon group velocity dependent on θ for the first and second $\boldsymbol{u}^-$ modes is shown in Fig. 4(e). At large θ, the phonon group velocities become the velocities of the transverse and longitudinal phonon modes of monolayer graphene. In the process of decreasing the angle, due to the formation of miniband, the phonon velocity decreases and approaches a constant value at a low angle limit. To explain it, a simple effective triangular lattice model was promoted and chemical bonds are seen as domain walls. The length change of the bonds and the total energy of the bonds were calculated. By this model, the phonon dispersion calculated is agree with Fig. 4(c). The important principle is that the potential energy of a bond (a domain wall) is proportional to its length, but not to the squared length. Besides, it is also found that in-plane phonon symmetric modes are hardly affected by the twist angle while in-plane phonon asymmetric modes are affected and minibands are formed. On the other hand, the minibands for phonons out-of-plane are not found and the density of states (DOS) of those remain unchanged. These results are expected to affect the thermal conductivity and phonon-related thermal phenomena in tBLGs.

3. Electron–phonon interaction in moiré superlattices

The new structure and period in the 2D van der Waals heterojunction will affect the phonons, electron–phonon, exciton–phonon, and phonon–phonon interactions of the 2D material that constitutes the heterojunctions and the heterojunction itself, exhibiting new characteristics. Fig. 5 shows the electron–phonon interaction in moiré superlattices, where the EPC is affected by the moiré patterns. Studying these many-body effects is important to understand the fundamental physical phenomena and explore potential applications in the moiré superlattice, such as superconductivity, super-Coulombic long-range dipolar interactions, and quantum emission[31]. Here, we discuss the moiré electron–phonon interaction in theory and sum up the recent studies including exciton–phonon coupling and thermoelectricity in moiré super-
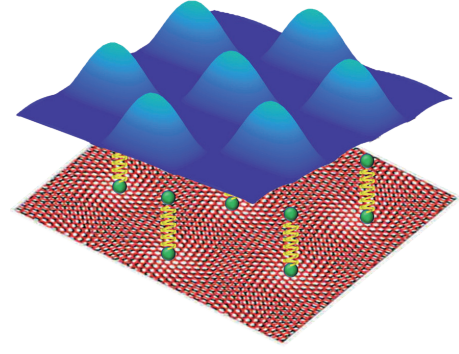

Fig. 5. (Color online) Illustration of the electron–phonon interaction in moiré superlattices. The springs representing phonons and a periodic electronic potential is on the top of the picture.

lattice. Such studies of phonon coupling are likely to pave the way for the exploration of new quantum phenomena in moiré patterns.

3.1. Electron–phonon interaction in moiré superlattices

The electron–phonon interaction in the moiré superlattice is caused by the intralayer part and the interlayer part, where the former is from the strain-induced pseudo-vector field, and the latter is from the change of the moiré pattern. In tBLG, the effect of moiré superlattice leads to the different interlayer asymmetric displacement vectors and changes the interlayer Hamiltonian. Next, the interlayer part of EPC is analyzed with interlayer Hamiltonian and Bloch bases at different layers. The intralayer Hamiltonian changes because of the shift of the pseudovector and the intralayer part of EPC is calculated with intralayer Hamiltonian and Bloch bases at the same layers. The interlayer and intralayer EPC strength $g_{n,\boldsymbol{q}}$ is introduced from the matrix element for EPC. And the averaged coupling amplitude $\bar{g}_n$ can be calculated. Considering the total EPC in tBLG, the Hamiltonian is written as[30]

$$H_{\mathrm{e-p}} = \frac{1}{\sqrt{S}}\sum_{naa'}\sum_{\boldsymbol{q}\boldsymbol{k}\boldsymbol{k}'\in \mathrm{MBZ}}\left(a_{n,\boldsymbol{q}}^\dagger + a_{n,-\boldsymbol{q}}\right)c_{a',\boldsymbol{k}'}^\dagger c_{a,\boldsymbol{k}} \times g_{n,\boldsymbol{q}}\left(a, \boldsymbol{k}; a', \boldsymbol{k}'\right), \quad (3)$$

where n is the mode index, $\boldsymbol{q}$ is the vector of the reciprocal superlattice. S is the unit area, $\boldsymbol{k}$ is the Bloch vector, a is the band index in the first moiré Brillouin zone, $c_{a,\boldsymbol{k}}^\dagger$ and $c_{a,\boldsymbol{k}}$ are respectively creation and annihilation operators of an electron, $a_{n,\boldsymbol{q}}^\dagger$ and $a_{n,-\boldsymbol{q}}$ are respectively creation and annihilation operators of the phonon, and $g_{n,\boldsymbol{q}}$ represents the EPC strength. The averaged coupling amplitude $\bar{g}_n$ is given by[30]

$$\bar{g}_n^2 \equiv \frac{1}{N_{\boldsymbol{q}}}\sum_{\boldsymbol{q}\in \mathrm{MBZ}}\frac{1}{4}\sum_{a=\pm, a'=\pm}\left|g_{n,\boldsymbol{q}}\left(a', \overline{K} + \boldsymbol{q}; a, \overline{K}\right)\right|^2, \quad (4)$$

where $N_{\boldsymbol{q}}$ is the number of sampling points of $\boldsymbol{q}$, and $\overline{K}$ is the position of the moiré Brillouin zone point $\overline{K}$. The twist angles-dependent $\bar{g}_n$ can be observed in Fig. 6 where the blue and red curves are the interlayer and intralayer contributions, respectively. The overall coupling amplitude increases as the twist angle decreases but the change of EPC with angle is not drastic. The superlattice hybridization is week and therefore, the monolayer eigenstate with a single wave component dominates every electron and phonon eigenstate. In the low-lying electronic states (composed of low K's),
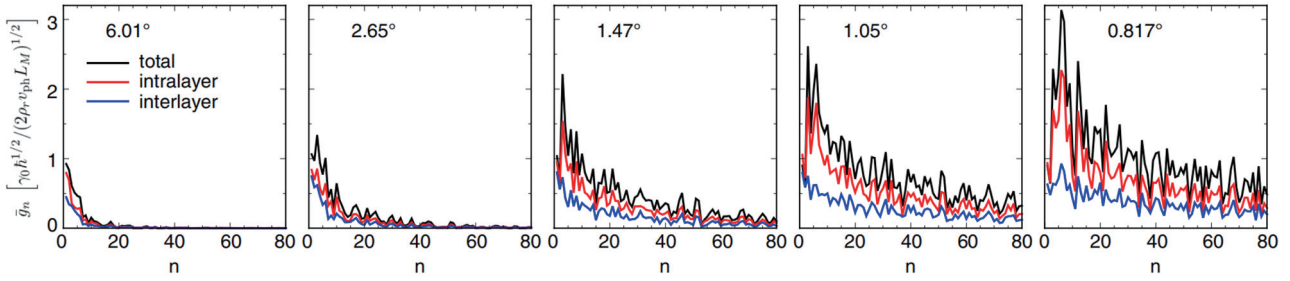
Fig. 6. (Color online) EPC strength $\bar{g}_n$ as a function of the phonon band index n in various twist angles. Reproduced with permission from Ref. [30]. Copyright 2020, American Physical Society.
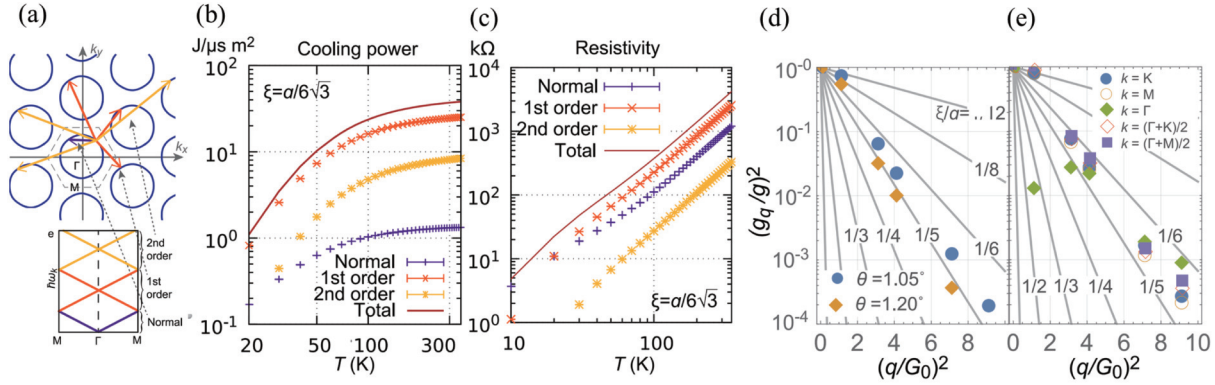

Fig. 7. (Color online) (a) Electron–phonon scattering in the extended Brillouin zone. The first Brillouin zone is shown as dashed hexagon marks; the blue circles are the Fermi surface. Yellow and orange arrows represent the umklapp processes and the purple arrow represents the normal processes. Both of them contribute to scattering. (b) Temperature dependence of the power of electron-lattice cooling for two different Wannier orbitals radii. (c) System resistivity and the resistivity from the sum of contributions from different phonon branches varying with the temperature of different electron–phonon processes. (d) At twist angles $\theta = 1.20°$ and $1.05°$, shape factors are shown for diamond and disk respectively, calculated of the continuum model at K points from the Wannier function. With different Wannier function ξ, the grey lines are shape factors g_q proportional to Gaussian functions $\exp(-\xi^2 q^2/4)$. (e) Shape factors at $\theta = 1.05°$ for different electron wave numbers $\boldsymbol{k}$. Reproduced with permission from Ref. [32]. Copyright 2021, ACS Publication.

the phonons of large phonon band index n's (mainly composed of high q) do not have related matrix elements, and this is why $\bar{g}_n$ decay quickly.

3.2. Enhancement of EPC in moiré superlattices

A prominent property of the graphene moiré superlattice is the reshaped Wannier orbital, the size of which can be tuned by the twist angle θ. The squeezing of the electron Wannier orbitals results in a much larger electron–phonon interaction strength than that in pristine monolayer graphene[32]. The enhanced interaction enables the scattering rate of the electron–phonon to exceed the expected value of the enhanced electron density of flat bands[33]. A toy model of moiré graphene is proposed[32] to explore the effect of compact Wannier orbitals on EPC. In the toy model, the honeycomb lattice periodicity and symmetry are matched to a moiré superlattice. The narrow band of honeycomb lattice is studied on a tight-binding approach, and Gaussian functions $\exp(-\xi^2 q^2/4)$ can model the compact Wannier orbitals, where ξ is the orbital radius. Then, the Hamiltonian of EPC is written as

$$H_{ep} = -\sum_{\boldsymbol{q},\boldsymbol{k},\boldsymbol{G},n} \frac{g_{\boldsymbol{q}+\boldsymbol{G}}}{\sqrt{V}} \sqrt{\hbar\omega_{\boldsymbol{q}+\boldsymbol{G}}} \hat{\psi}^\dagger_{\overline{\boldsymbol{k}+\boldsymbol{q}},n} \hat{\psi}_{\boldsymbol{k},n} \left(\hat{a}_{\boldsymbol{q}+\boldsymbol{G}} + \hat{a}^\dagger_{-\boldsymbol{q}-\boldsymbol{G}}\right), \quad (5)$$

where $\boldsymbol{q}$ is the vector of the reciprocal superlattice, $\boldsymbol{k}$ is the electron momentum, $\boldsymbol{G}$ is the vector of the moiré reciprocal lattice, n is the order of scattering, V is the area of the system, ω

is the angular frequency of phonons, $a^\dagger_q$ and a_q are respectively annihilation and creation operators of the phonon, $\hat{\psi}$ is a spinor in sublattice-valley space. The modulation of the EPC is described by a form factor $g_{\boldsymbol{q}+\boldsymbol{G}} = g e^{-(\boldsymbol{q}+\boldsymbol{G})^2\xi^2/4}$. Reciprocal lattice vector $\boldsymbol{G} \neq 0$ suggests moiré superlattice potential raising electron Bragg scattering, so Wannier orbital localization is formed and EPC is enhanced.

Some plane waves with the form $\exp(i(\boldsymbol{k} + \boldsymbol{G}) \cdot \boldsymbol{r})$ compose Wannier functions in tBLG suggesting a large umklapp scattering amplitude, where the reciprocal vector of moiré superlattice changes electron momentum. Fig. 7(a) shows different electron–phonon scattering containing different umlapp processes. Electron cooling and resistivity are highly sensitive to the nature of electron–phonon umklapp scattering. Figs. 7(b) and 7(c) show the temperature dependence of cooling power and resistivity with contributions of the second-order umklapp, first-order umklapp, and normal processes calculated by the model above, which manifests enhanced electron–phonon interaction. To further confirm the validity of the toy model, it is compared with the continuum model of moiré graphene. Figs. 7(d) and 7(e) show the form factor of the EPC calculated with the continuum model (diamond and disk symbols) and toy model (gray line). The law of form factor changes with predictedmomentum at different angles by the continuum model in Fig. 7(d) is consistent with the g_q calculated above. The best fitting results for the microscopic calculations using tightly localized Wannier orbitals support
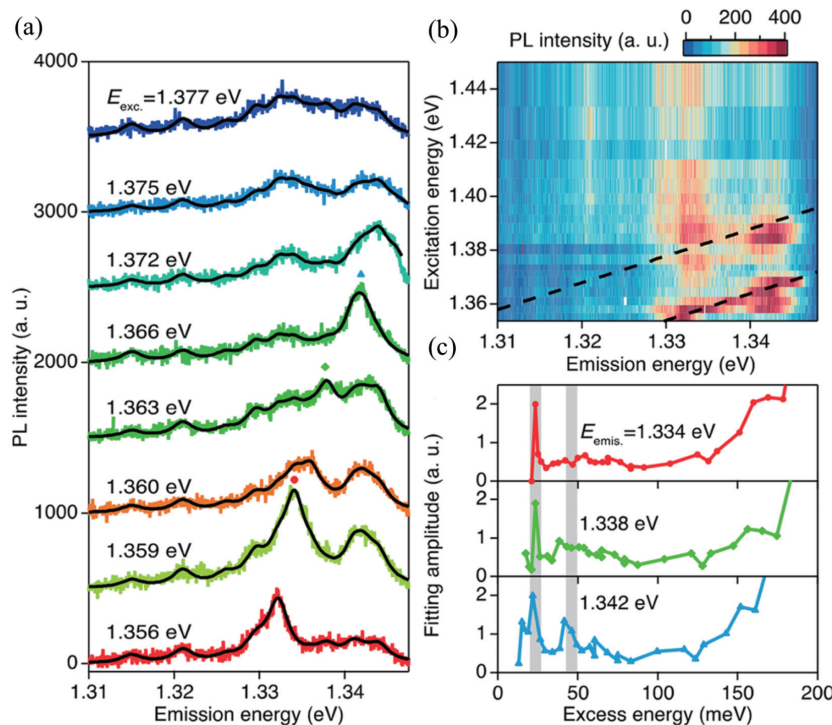
Fig. 8. (Color online) (a) PL spectra obtained measured from 1.356 to 1.377 eV in case of near-resonant excitation. Lorentzian functions filled are shown as black lines. (b) 2D PLE intensity map. The excess energy at 24 and 48 meV is shown with sloping black dashed lines. (c) Lorentzian fitted PLE spectra as a function of the excess energy of the PL spectra. The gray areas mean excess energy at 48 and 24 meV. Reproduced with permission from Ref. [35]. Copyright 2021, ACS Publication.

the Purcell-like enhancement of the electron–phonon scattering rate since the localization of the Wannier orbitals. In Fig. 7(e), the changing trend of g_q at different wavenumber $\boldsymbol{k}$ is similar to that using continuum model at different θ. This is because the charge distribution of the eigenstate at the Γ point is different with various wavenumbers. Therefore, the toy model is effective for calculating the form factor g_q in tBLGs.

Besides, the phonon also interacts with moiré excitons in 2D van der Waals heterostructures such as $MoSe_2$/WSe_2[34, 35], which can be reflected by near-resonant photoluminescence excitation (PLE) spectroscopy. To get near-resonant photoexcitation conditions, photoluminescence (PL) spectra need to be detected first. The PL spectra under various excitation energies are shown in Fig. 8(a). The energy of emission and resonance excitation for moiré exciton is around 1.33 and 1.36 eV, respectively. To observe PLE and PL more intuitively, the various excitation energies of Fig. 8(a) are given as vertical axis in Fig. 8(b). We can see the difference between excitation energies and emission energy have two typical values: 24 and 48 meV, shown as black dashed lines. To discuss the resonance features quantitatively, Lorentz functions are used to fit the spectra (Fig. 8(c)). The energy difference of 24 meV is close to the energy of A_1' phonon modes in $MoSe_2$ and the $A_1' + E_1$ phonon modes (~30 meV) in WSe_2 observed by Raman spectra, indicating that exciton–phonon coupling can explain this result. The slight difference between 24 meV and the energy of the phonon in Raman spectra is because of the different excitation processes of the phonon in the PLE measurement and Raman. For the interaction between the moiré exciton and phonon, the wave function of moiré excitons is supposed to expand in momentum space. In this case, the phonon modes with large wave numbers and Γ point can interact

with moiré exciton, which is in good agreement with the above measurements. This research reveals new physical phenomena of moiré exciton and phonon coupling.

3.3. Thermoelectricity in moiré superlattice

Moiré patterns affect the contribution of electron–phonon scattering to the cross-plane transport of electrons, which influences thermoelectric performance in twist 2D materials. The coupling of the two graphene layers in tBLGs varies strongly with the twist angle. For the large twist angle, the layers are essentially decoupled at low temperatures, but get effectively re-coupled at higher temperatures when the interlayer phonons drive cross-plane electrical transport through strong electron–phonon scattering[36]. Mahapatra et al. found a novel phonon-drag effect driving thermopower in tBLG, which is related to the twist angle[26]. In thermoelectric phenomena, the Seebeck coefficient is a measure of the magnitude of an induced thermoelectric voltage in response to a temperature difference between two different conductors or semiconductors. For the quadratic dispersion relation of layer breathing mode branch of phonons, Fig. 9(a) shows the Seebeck coefficient S of thermoelectric power with different twist angles depending on temperature. S varies linearly with T at low twist angles while similar nonmonotonic thermoelectric power was observed at large twist angles. When the twist angle is small, the generic electron–phonon scattering timescale shows weak dependence on θ due to the quadratic dispersion of phonon energy. However, when the twist angle is increased, the interlayer electronic tunneling timescale decays rapidly and becomes slower than the scattering timescale. To explain further, the electron–phonon scattering from the hybridized phonons drives the cross-plane thermoelectric transport at large twist angles, which results in an unconventional
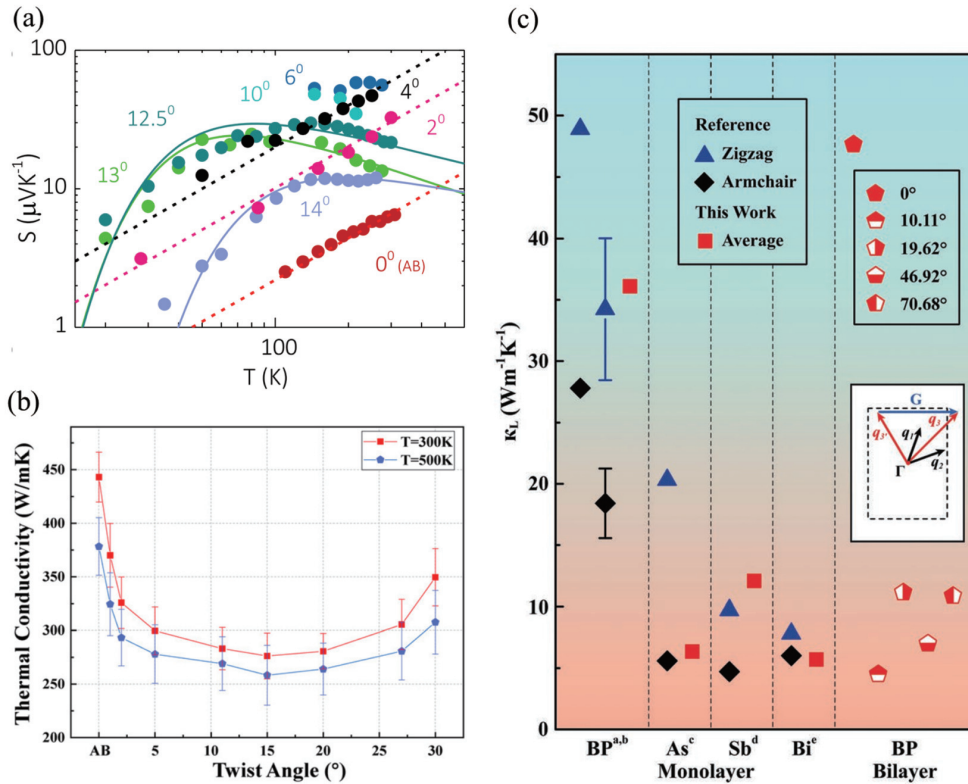
Fig. 9. (Color online) (a) Cross-plane thermoelectricity with different twist angles. The dotted lines show the linear T dependence of thermoelectric power. The solid lines show the fit of the thermoelectric power driven by phonons. Reproduced with permission from Ref. [26]. Copyright 2020, American Physical Society. (b) The thermal conductivity depending on twist angles of different temperatures. Reproduced with permission from Ref. [25]. Copyright 2021, AIP Publishing. (c) Calculated lattice thermal conductivities of tbBPs at 300 K with various twist angles at 300 K. Reproduced with permission from Ref. [37]. Copyright 2022, Wiley Publishing.

phonon-drag effect at the sub-nanometer distance. Furthermore, Han *et al.* measured thermal conductivity (κ) in the suspended single crystalline tBLG domains with various interlayer twist angles via the optothermal Raman technique[25]. In Fig. 9(b), κ exhibits an asymmetrical V-shaped dependence on the interlayer twist angle. It was confirmed that the enhancement of the phonon scattering affects the in-plane thermal conduction by further analysis of the vibrational density of states. Besides, the angle-dependent thermoelectric properties of twisted bilayer black phosphorene (tbBP) by first-principles calculations are reported[37]. The lattice thermal conductivities of the tbBPs are significantly reduced in comparison with pristine bilayer black phosphorene by almost an order of magnitude, especially when the twist angle is 10.11° and 46.92° (Fig. 9(c)). Such highly depressed lattice thermal conductivity can be attributed to the reduced Debye temperature and the strong anharmonic phonon scattering induced by the moiré superlattices. These studies provide new ways to optimize thermoelectric performance by tuning the moiré superlattice in low-dimensional materials.

4. Phonon-mediated superconductivity in moiré superlattices

The unconventional superconductivity in 2D superlattices has been reported in tBLGs with a specific angle called the "magic angle"[7]. By stacking two graphene layers with a magic angle of 1.08° and regulating the carrier concentration through the gate voltage (Fig. 10(a)), Cao *et al.* successfully achieved a Mott-like insulator with a half-filling state[7], and

subsequently, high-temperature superconductivity similar to that in copper oxides is exhibited at 1.7 K (Fig. 10(b)). It is the first time to achieve superconductivity in pure carbon-based two-dimensional materials, which has important implications for the research of high-temperature superconductivity mechanisms and the exploration of the frontier problems in strongly correlated electronic materials. Recently, strong EPC has been found in tBLGs which spires interest in phonon-mediated superconductivity[15, 22, 38, 39]. Superconductivity in tBLGs was experimentally demonstrated associated with moiré patterns[23, 24]. The study of the EPC of different flat-band states in moiré graphene has important implications for the superconducting mechanism. In addition, topological surface states are also found in moiré superlattices, which can enhance the superconductivity.

4.1. Phonon-mediated superconductivity in magic-angle graphene

There are various theoretical models to explain the superconductivity in moiré superlattices in magic-angle tBLGs such as phonon-mediated mechanism[22], minimal Hubbard model for electronically driven superconductivity[41], two-orbital Hubbard model on an emergent honeycomb lattice[42], the low-energy tight-binding model for the four narrow bands of tBLG and so on[43]. Here we focus on the phonon-mediated electron–electron attractive interaction in s-wave and d-wave pairing channels[22]. The s- and d- here refer to the angular quantum numbers of electron orbitals and in superconductivity, the pairing of them represents the angular quantum numbers of Cooper pairs. By introducing continuum moiré Hamilto-
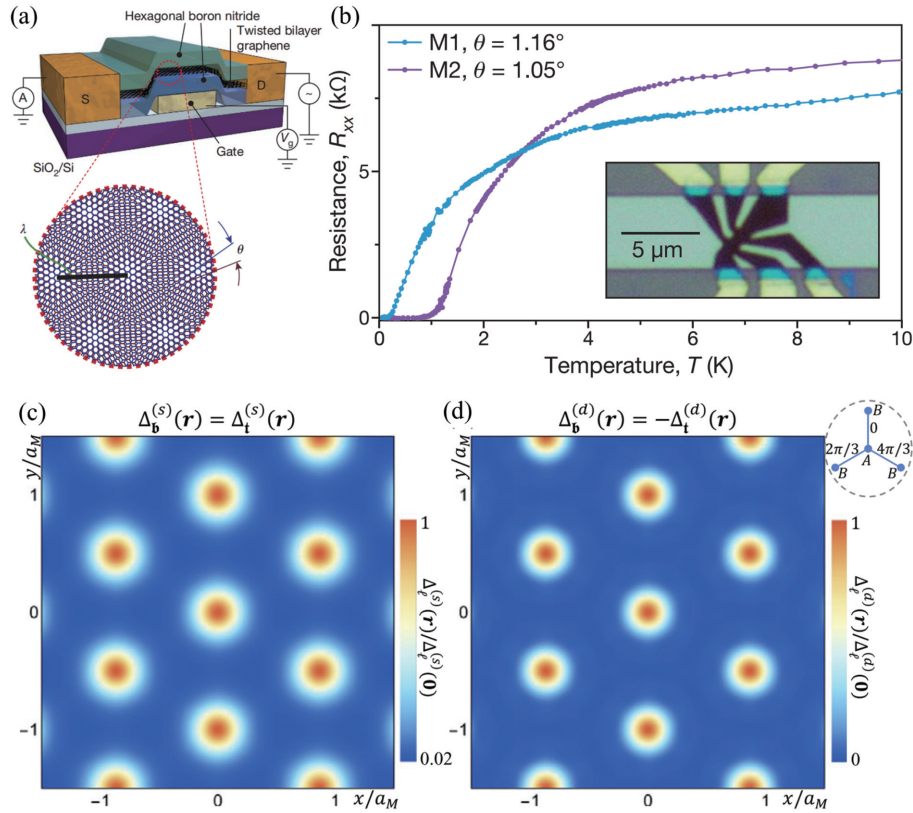
Fig. 10. (Color online) (a) Schematic of the tBLG devices fabricated on SiO₂/Si substrates. (b) Current–voltage curves of two devices M1 and M2 measured in graphene superlattices and at different temperatures. Resistance R_{xx} was measured in two devices, with $\theta = 1.05°$ and $1.16°$, respectively. Reproduced with permission from Refs. [7, 40]. Copyright 2018, Nature. (c) Real-space map of pair amplitudes $\Delta(r)$ that satisfy s-wave linearized gap equations. (d) Real-space map of pair amplitudes $\Delta(r)$ that satisfy d-wave linearized gap equations. In (c) and (d), chemical potential $\mu = -0.3$ meV and twist angle $\theta = 1.05°$. Reproduced with permission from Ref. [22]. Copyright 2018, American Physical Society.

nian for low-energy electrons and the effect of phonons by EPC Hamiltonian. The phonon-mediated interaction Hamiltonian can be derived

$$H_{\text{attractive}} = -\int \text{d}^2 \boldsymbol{r} \left\{ g_{E_2} \left[\left(\hat{\psi}^\dagger \tau_z \sigma_y \hat{\psi} \right)^2 + \left(\hat{\psi}^\dagger \sigma_x \hat{\psi} \right)^2 \right] \right.$$
$$\left. + g_{A_1} \left[\left(\hat{\psi}^\dagger \tau_x \sigma_x \hat{\psi} \right)^2 + \left(\hat{\psi}^\dagger \tau_y \sigma_x \hat{\psi} \right)^2 \right] \right\}, \quad (6)$$

where $\hat{\psi}$ is a spinor in sublattice-valley space, and $\tau_{x,y,z}$ and $\sigma_{x,y,z}$ are Pauli matrices in valley space and sublattice space, respectively. The attractive interaction strength g mediated by phonons is obtained[22]

$$g_a = \frac{A}{N} \left(\frac{F_a}{\hbar \omega_a} \right)^2 \frac{\hbar^2}{2M}, \quad (7)$$

where a represents phonon modes and A is the sample area, N is the number of sites of modes in a monolayer, F is coupling constants, and M is the mass of a single carbon atom. In addition, the phonon-mediated electron-electron interaction Hamiltonian is restricted to the Bardeen-Cooper-Schrieffer (BCS) channel. In Figs. 10(c) and 10(d), s-wave and d-wave pairing in real space of tBLM are shown. The pair amplitude $\Delta(r)$ of s-wave concentrated near AA regions in the moiré pattern and is layer independent. In the normal state of the flat bands, the spatial variation of $\Delta(r)$ follows the electron density distribution. $\Delta(r)$ transforms trivially under all the point-group symmetries, confirming that intra-sublattice pairing is s-wave pairing. At the atomic scale, chiral d-wave pairing is

realized by forming nearest-neighbor spin-singlet Cooper pairs with bond-dependent phase factors. $\Delta(r)$ of d-wave shows the center-of-mass motion of the Cooper pairs, while the relative motion of the two paired electrons has d-wave symmetry. Therefore, a general framework of superconducting pairing with attractive electron–electron mediated by phonons was set up and this is expected to be an important step towards a complete quantitative theory of tBLGs. It should be noted that, up to now, which mechanism responsible for the superconductivity in moiré superlattices is under debate and needs further experimental verification.

4.2. Moiré surface states and enhanced superconductivity

Superconductivity can be mediated and enhanced by moiré phonons. Van Hove singularities present in the moiré surface electronic states are found[44], which lead to different DOS[23]. In the case of phonon-mediated electron–electron attraction, some of these Van Hove singularities exhibit a power-law divergent DOS, termed higher-order Van Hove singularities, where superconductivity is enhanced by the power-law divergent DOS. The delayed electron–phonon interaction λ^* associated with the power law can be revealed by the electron–phonon superconducting critical temperature T_c with a new analytical formula for[23]

$$T_c = \frac{\Lambda}{l(v)^{1/v}} \left[\frac{1}{\lambda - \mu^*} - \log\left(\frac{\varepsilon_D}{\Lambda} \right) + \frac{1}{|v|} \right]^{-1/|v|}, \quad (8)$$

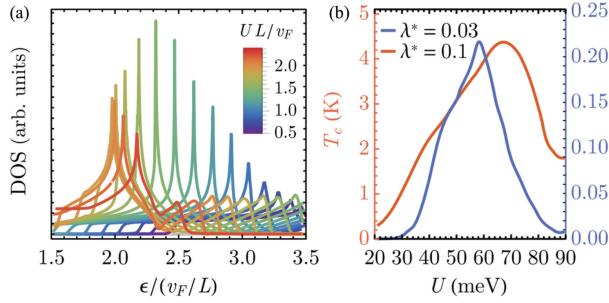**Z Y Li et al.: Review of phonons in moiré superlattices**

Fig. 11. (Color online) (a) Moiré surface state DOS with sharp higher-order Van hove singularities-like peaks at C_6 potential with various potential U[23]. (b) Transition temperature T_c at $v_F/L = 435$ K and $\varepsilon_D = 80$ K for different potential U. The blue axis on the right and red axis on the left correspond to the T_c, which shows broad peaks corresponding to higher-order Van Hove singularities around potentials. Reproduced with permission from Ref. [23]. Copyright 2021, American Physical Society.

where $0 > \nu > -1$ expresses the power-law exponent of the DOS, Λ is the high-order Van Hove singularities peak cutoff, ε_D is the Debye frequency, μ^* is the screened repulsion, $I(\nu) = 2(2^{1-\nu} - 1)\Gamma(\nu)\xi(\nu)$, $\xi(\nu)$ and $\Gamma(\nu)$ are the Riemann ξ function and Γ function, respectively. Eq. (8) generalizes the BCS formula. The analytical nature of this formula shows that when the λ^* value is small, the superconductivity is significantly enhanced compared with that of ordinary metals and ordinary Van Hove singularities.

Over a wide range of U, the strength of periodic scalar potential, the DOS has a sharp high-order-Van Hove singularities-like peak (Fig. 11(a)), which means the power-law diverging behavior of the DOS still exists and superconductivity is enhanced. In Fig. 11(b), U-dependent T_c is calculated by gap equation with the chemical potential held exactly at the Van Hove singularities. Over a wide range of U, T_c is enhanced and when λ^* is large, the window of U with enhancement is wide. It is shown that the energy difference between the Van Hove singularities and the local maxima or minima is on the order of sub-Kelvin even at tens of megavolts away from the higher-order Van Hove singularities. It means that the superconductivity enhancement is persists and robust though the system is perturbed away from high-order Van Hove singularities.

4.3. Relevance between robust superconductivity and strong EPC in graphene moiré superlattices

Graphene moiré superlattice is a superior platform to study superconductivity but robust superconductivity is only found in some types of twist graphene-like tBLGs and tTLGs, which raises a question on superconducting mechanism. EPC in graphene moiré superlattices also exhibits similar differences. In an atomic calculations study of the EPC of graphene moiré superlattices and electronic structure, it can be demonstrated that tBLG and tTLG have strong EPC (coupling strength $\lambda > 1$) at their magic angles, while twisted monolayer-bilayer graphene (tMBLG) and twisted double bilayer graphene (tDBLG) are an order of magnitude weaker. We show the superconducting transition temperature T_c depending on EPC strength derived by the Eliashberg equation[45]. If the dispersion of the phonon modes and the energy dependence of the electronic DOS are ignored, the explicit T_c formula-

Table 1. Electron–phonon coupling strength λ_i, mode-resolved. Reproduced with permission from Ref. [24]. Copyright 2021, American Physical Society.

Condition	λ_i (tBLG)	λ_i (tTLG)	λ_i (tDBLG)	λ_i (tMBLG)
$\omega_i = 10$ meV	0.297	0.233	0.064	0.037
$\omega_i = 167$ meV	0.914	0.743	0.026	0.045
$\omega_i = 197$ meV	0.648	0.532	0.018	0.030

Table 2. T_c and D calculated for tBLG, tTLG, tDBLG, and tMBLG. Reproduced with permission from Ref. [24]. Copyright 2021, American Physical Society.

Parameter	tBLG	tTLG	tDBLG	tMBLG
D (meV)	0.53	0.67	3.4	6.7
T_c ($\mu = 0.15$) (K)	3.33	3.55	0.0	0.0
T_c ($\mu = 0.05$) (K)	3.45	3.67	10^{-7}	10^{-6}

tion for the half-filled band can be derived as[24]

$$T_c = \prod_i \left(\frac{\omega_i D}{\omega_i + D}\right)^{\lambda_i/\lambda} \exp\left(-\frac{1 + \tilde{\lambda}}{\lambda - \mu^*}\right), \tag{9}$$

where λ_i and ω_i are the EPC strength and the energy of the i-th phonon mode, D is the half-bandwidth, $\mu^* = \mu \Big/ \left(\mu \sum_i \ln(D/\omega_i + 1)^{\lambda_i/\lambda} + 1\right)$ is the Coulomb pseudopotential, $\tilde{\lambda} = 2 \sum_i \lambda_i D/(D + \omega_i)$ is the mass renormalization constant. The λ_i with different ω_i is shown in Table 1. Take them to Eq. (9) and the critical temperature T_c can be obtained as shown in Table 2. The calculated T_c results for the half-filled Fermi energy of the electron- (hole-) side flat bands of tBLG and tTLG (tDBLG and tMBLG) agree well with the experimental observations[7, 46, 47]. These results show a correlation between experimental observations providing a deeper understanding of the graphene moiré superlattice.

5. Conclusion

Interlayer coupling in twisted bilayer 2D materials induces periodic moiré potentials that alter the lattice vibrations of the monolayer components to form moiré phonons[48]. The moiré phonons of the twisted bilayer 2D materials can be used to map the phonon dispersion of the monolayer components by varying the twist angle. The strong interaction between the atomic reconstruction of the moiré pattern and various phonon modes can lead to the reconstruction of phonons in the small twist angle range, which can be observed by Raman spectroscopy. In addition, the electron–phonon, exciton–phonon, and photon–phonon interactions are affected by moiré patterns, where the enhancement of electron–phonon interactions can be observed. EPC is predicted to mediate superconductivity in moiré superlattices and achieve superconductivity enhancement.

The study of moiré phonon provides a deeper understanding of novel physical phenomena such as EPC and superconductivity, which promotes further investigations regarding phonons in moiré superlattices such as the effect of electron–phonon interactions on metal–insulator transitions, magnetic order, and Wigner crystal state stability in transition metal dichalcogenides moiré materials[21]. The twist-con-

trolled thermoelectricity in moiré superlattices raised by phonon scattering can not only probe the interlayer coherent states in twisted 2D material but may trigger new thermoelectric designs[26]. Furthermore, the research related to moiré phonons is beneficial to further explore new quantum phenomena in the moiré pattern and promote their applications. The studies of exciton–phonon interaction and phonon polariton in moiré superlattices open the possibility for novel quantum emitters[49] in 2D semiconductor heterostructures.

Acknowledgements

References

[1]   Encyclopedia Britannica. Chicago: British Encyclopedia Publishing Company, 2022

[2]   Kobayashi K. Moiré pattern in scanning tunneling microscopy: Mechanism in observation of subsurface nanostructures. Phys Rev B, 1996, 53, 11091

[3]   N'Diaye A T, Bleikamp S, Feibelman P J, et al. Two-dimensional Ir cluster lattice on a graphene moiré on Ir(111). Phys Rev Lett, 2006, 97, 215501

[4]   Liu Y, Weiss N O, Duan X D, et al. Van der Waals heterostructures and devices. Nat Rev Mater, 2016, 1, 16042

[5]   Lopes Dos Santos J M B, Peres N M R, Castro Neto A H. Graphene bilayer with a twist: Electronic structure. Phys Rev Lett, 2007, 99, 256802

[6]   Bistritzer R, MacDonald A H. Moire bands in twisted double-layer graphene. Proc Natl Acad Sci USA, 2011, 108, 12233

[7]   Cao Y, Fatemi V, Fang S A, et al. Unconventional superconductivity in magic-angle graphene superlattices. Nature, 2018, 556, 43

[8]   Huang D, Choi J, Shih C K, et al. Excitons in semiconductor moiré superlattices. Nat Nanotechnol, 2022, 17, 227

[9]   Schmitt D, Bange J P, Bennecke W, et al. Formation of moiré interlayer excitons in space and time. Nature, 2022, 608, 499

[10]   Tran K, Moody G, Wu F C, et al. Evidence for moiré excitons in van der waals heterostructures. Nature, 2019, 567, 71

[11]   Jin C H, Regan E C, Yan A M, et al. Observation of moiré excitons in WSe$_2$/WS$_2$ heterostructure superlattices. Nature, 2019, 567, 76

[12]   Yan J A, Ruan W Y, Chou M Y. Phonon dispersions and vibrational properties of monolayer, bilayer, and trilayer graphene: Density-functional perturbation theory. Phys Rev B, 2008, 77, 125401

[13]   Nika D L, Balandin A A. Phonons and thermal transport in graphene and graphene-based materials. Rep Prog Phys Phys Soc G B, 2017, 80, 036502

[14]   Ribeiro-Palau R, Zhang C J, Watanabe K, et al. Twistable electronics with dynamically rotatable heterostructures. Science, 2018, 361, 690

[15]   Choi Y W, Choi H J. Strong electron-phonon coupling, electron-hole asymmetry, and nonadiabaticity in magic-angle twisted bilayer graphene. Phys Rev B, 2018, 98, 241412

[16]   Jiang J W, Wang B S, Rabczuk T. Acoustic and breathing phonon modes in bilayer graphene with Moiré patterns. Appl Phys Lett, 2012, 101, 023113

[17]   Cocemasov A I, Nika D L, Balandin A A. Phonons in twisted bilayer graphene. Phys Rev B, 2013, 88, 12

[18]   Angeli M, Tosatti E, Fabrizio M. Valley jahn-teller effect in twisted bilayer graphene. Phys Rev X, 2019, 9, 041010

[19]   Lin M L, Tan Q H, Wu J B, et al. Moiré phonons in twisted bilayer MoS$_2$. ACS Nano, 2018, 12, 8770

[20]   Koshino M, Son Y W. Moiré phonons in twisted bilayer graphene. Phys Rev B, 2019, 100, 075416

[21]   Quan J M, Linhart L, Lin M L, et al. Phonon renormalization in reconstructed MoS$_2$ moiré superlattices. Nat Mater, 2021, 20, 1100

[22]   Wu F C, MacDonald A H, Martin I. Theory of phonon-mediated superconductivity in twisted bilayer graphene. Phys Rev Lett, 2018, 121, 257001

[23]   Wang T G, Yuan N F Q, Fu L. Moiré surface states and enhanced superconductivity in topological insulators. Phys Rev X, 2021, 11, 021024

[24]   Choi Y W, Choi H J. Dichotomy of electron-phonon coupling in graphene moiré flat bands. Phys Rev Lett, 2021, 127, 167001

[25]   Han S, Nie X H, Gu S Z, et al. Twist-angle-dependent thermal conduction in single-crystalline bilayer graphene. Appl Phys Lett, 2021, 118, 193104

[26]   Mahapatra P S, Ghawri B, Garg M, et al. Misorientation-controlled cross-plane thermoelectricity in twisted bilayer graphene. Phys Rev Lett, 2020, 125, 226802

[27]   Wiki. Moiré pattern, 2022, https://en.wikipedia.org/wiki/Moir%C3%A9_pattern#Materials_science_and_condensed_matter_physics

[28]   Jung J, Raoux A, Qiao Z H, et al. *Ab initio* theory of moiré superlattice bands in layered two-dimensional materials. Phys Rev B, 2014, 89, 205414

[29]   San-Jose P, Gutiérrez-Rubio A, Sturla M, et al. Spontaneous strains and gap in graphene on boron nitride. Phys Rev B, 2014, 90, 075428

[30]   Koshino M, Nam N N T. Effective continuum model for relaxed twisted bilayer graphene and moiré electron-phonon interaction. Phys Rev B, 2020, 101, 195425

[31]   Lai J M, Farooq M U, Sun Y J, et al. Multiphonon process in Mn-doped ZnO nanowires. Nano Lett, 2022, 22, 5385

[32]   Ishizuka H, Fahimniya A, Guinea F, et al. Purcell-like enhancement of electron-phonon interactions in long-period superlattices: Linear-temperature resistivity and cooling power. Nano Lett, 2021, 21, 7465

[33]   Sun Z X, Hu Y H. How magical is magic-angle graphene. Matter, 2020, 2, 1106

[34]   Tan P H. Signatures of moiré excitons. J Semicond, 2019, 40, 040202

[35]   Shinokita K, Miyauchi Y, Watanabe K, et al. Resonant coupling of a moiré exciton to a phonon in a WSe$_2$/MoSe$_2$ heterobilayer. Nano Lett, 2021, 21, 5938

[36]   Mahapatra P S, Sarkar K, Krishnamurthy H R, et al. Seebeck coefficient of a single van der waals junction in twisted bilayer graphene. Nano Lett, 2017, 17, 6822

[37]   Duan S, Cui Y, Yi W, et al. Enhanced thermoelectric performance in black phosphorene via tunable interlayer twist. Small, 2022, 2204197

[38]   Peltonen T J, Ojajärvi R, Heikkilä T T. Mean-field theory for superconductivity in twisted bilayer graphene. Phys Rev B, 2018, 98, 220504

[39]   Lian B, Wang Z J, Bernevig B A. Twisted bilayer graphene: A phonon-driven superconductor. Phys Rev Lett, 2019, 122, 257002

[40]   Cao Y, Fatemi V, Demir A, et al. Correlated insulator behaviour at half-filling in magic-angle graphene superlattices. Nature, 2018, 556, 80

[41]   Xu C K, Balents L. Topological superconductivity in twisted multilayer graphene. Phys Rev Lett, 2018, 121, 087001

[42]   Yuan N F Q, Fu L. Model for the metal-insulator transition in graphene superlattices and beyond. Phys Rev B, 2018, 98, 045103

[43]   Kang J, Vafek O. Symmetry, maximally localized wannier states, and a low-energy model for twisted bilayer graphene narrow bands. Phys Rev X, 2018, 8, 031088

[44]   Witt N, Pizarro J M, Berges J, et al. Doping fingerprints of spin and lattice fluctuations in moiré superlattice systems. Phys Rev B, 2022, 105, L241109

[45] Sadovskii M V. Antiadiabatic phonons, coulomb pseudopotential, and superconductivity in eliashberg—McMillan theory. Jetp Lett, 2019, 109, 166

[46] Hao Z Y, Zimmerman A M, Ledwith P, et al. Electric field-tunable superconductivity in alternating-twist magic-angle trilayer graphene. Science, 2021, 371, 1133

[47] Park J M, Cao Y, Watanabe K, et al. Tunable strongly coupled superconductivity in magic-angle twisted trilayer graphene. Nature, 2021, 590, 249

[48] Cong X, Lin M L, Tan P H. Lattice vibration and Raman scattering of two-dimensional van der Waals heterostructure. J Semicond, 2019, 40, 091001

[49] Zhou Z Q, Cui Y, Tan P H, et al. Optical and electrical properties of two-dimensional anisotropic materials. J Semicond, 2019, 40, 061001

Jia-Min Lai is now a Ph.D. student supervised by Prof. Jun Zhang in the State Key Laboratory of Superlattices and Microstructures, Institute of Semiconductors, Chinese Academy of Sciences. She received her bachelor's degree from Northeastern University in China. Her current research interest focuses on electron–phonon coupling in semiconductors.

Zhenyao Li is now a M.S. student supervised by Prof. Jun Zhang in the State Key Laboratory of Superlattices and Microstructures, Institute of Semiconductors, Chinese Academy of Sciences. He received his bachelor's degree from Nankai University in China. His current research interest focuses on quantum optomechanics.

Jun Zhang received a bachelor's degree from Inner Mongolia University in China in 2004, and a Ph.D. from the Institute of Semiconductors, Chinese Academy of Sciences in 2010. Then he worked as a postdoctoral fellow at Nanyang Technological University in Singapore from 2010 to 2015 and joined the State Key laboratory of Superlattice for Semiconductors (CAS) as a professor in 2015. His current researches focus on light-matter interactions in semiconductor materials including Raman and Brillouin scattering, and laser cooling in semiconductors.